


Investigation of the SiO₂-SiC Interface Using Low-Energy Muon-Spin-Rotation Spectroscopy

Piyush Kumar^{1,*}, Maria Inês Mendes Martins^{1,2}, Marianne Etzelmüller Bathen¹, Judith Woerle¹, Thomas Prokscha², and Ulrike Grossner¹

¹Advanced Power Semiconductor Laboratory, Eidgenössische Technische Hochschule Zürich, Physikstrasse 3, Zurich 8092, Switzerland

²Laboratory for Muon Spin Spectroscopy, Paul Scherrer Institute, Forschungsstrasse 111, Villigen PSI 5232, Switzerland

 (Received 23 November 2022; revised 10 February 2023; accepted 4 April 2023; published 8 May 2023)

Using positive muons as local probes implanted at low energy enables gathering information about the material of interest with nanometer-depth resolution (low-energy muon-spin-rotation spectroscopy, LE μ SR). In this work, we leverage the capabilities of LE μ SR to perform a detailed investigation of the widely studied yet poorly understood SiO₂-SiC interface. Thermally oxidized samples are investigated before and after annealing in nitric oxide (NO) and argon (Ar) environment. Thermal oxidation is found to result in structural changes both in the SiC crystal close to the interface and at the interface itself, which severely degrade the transport properties of charge carriers. Annealing in NO environment is known to passivate the defects leading to a reduction of the density of interface traps (D_{it}); LE μ SR further reveals that the NO annealing results in a thin layer of high carrier concentration in SiC, extending to more than 50 nm depending on the annealing conditions. From our measurements, we see indications of Si vacancy (V_{Si}) formation in SiC after thermal oxidation. Following NO annealing, nitrogen occupies the V_{Si} sites, leading to the well-documented reduction in D_{it} and, at the same time, creating a charge-carrier-rich region near the interface. The LE μ SR technique sheds light on the near-interface region in the SiO₂-SiC system, which is challenging to access using other techniques. By comparing the LE μ SR data from a sample with known doping density, we perform a high-resolution quantification of the free carrier concentration near the interface after NO annealing and discuss the origin of the observed near-surface variations. Finally, the depletion of carriers in a MOS capacitor in the region exactly below the interface is demonstrated using LE μ SR. The NO-annealed sample shows the narrowest depletion region, likely due to the reduced density of interface traps and the charge-carrier-rich region near the interface. Our findings demonstrate the many benefits of LE μ SR to study critical regions of semiconductor devices that have been inaccessible with other techniques, while simultaneously retaining both nanoscale-depth resolution and a nondestructive approach.

DOI: [10.1103/PhysRevApplied.19.054025](https://doi.org/10.1103/PhysRevApplied.19.054025)

I. INTRODUCTION

Muon-spin-rotation (μ SR) spectroscopy is a powerful technique capable of studying intricate properties of materials from various disciplines, such as superconductivity, magnetism, semiconductor defect characterization, physical chemistry, and dynamics of soft matter [1–5].

Positive muons (μ^+) act as microscopic probes and gather information about the region in the material in which they decay after implantation. For magnetic materials, the μ SR method has been successful in extracting the magnetic order parameter and magnetic volume fractions of the system and studying the dynamics of the magnetic

moments in a sample [6–8], whereas for various unconventional superconductors, it has been used to understand the relation and coexistence between magnetism and superconductivity [9,10]. μ SR also finds special applications in the field of semiconductors, where muons can replicate the behavior of hydrogen-related defects, which otherwise are challenging to probe [2–4].

A recent study with low-energy (LE) μ SR on germanium showed that charge-carrier profiles can be determined in the accumulation and depletion regions near the surface [11], whereas in silicon carbide (SiC), the sensitivity of the μ SR signal to defects created by proton irradiation has been demonstrated [12,13]. The sensitivity of μ SR to useful semiconductor parameters combined with the nanoscale resolution of the technique mark its

*kumar@aps.ee.ethz.ch

low-energy mode as an intriguing choice for investigating device-related interface and surface regions.

4H-SiC is among the most prominent and well-known semiconducting materials in the world of power semiconductor devices. Exhibiting a wide band gap, high thermal conductivity and high saturation velocity, SiC holds the key to creating efficient high-power devices [14]. With the research moving swiftly from silicon to other competing materials, SiC offers the advantage that it is the only compound semiconductor with SiO₂ as its native oxide [15]. In addition to being thermally stable and possessing high permittivity, SiO₂ is especially useful as it allows SiC devices to be fabricated with minor modifications to the already functional silicon (Si) fabrication facilities [16]. However, the concentration of thermal-oxidation-induced defects are at least one order of magnitude higher for SiC than its Si counterpart [15]. These defects are present at and near the interface and can have a debilitating impact on the carrier transport, leading to a high channel resistance. For a medium power device such as a 1.2-kV SiC power MOSFET, the channel resistance can contribute to as much as 60% of the total on-state resistance [17]. Although annealing in a NO environment is known to reduce the density of interface traps (D_{it}) [18], neither the defects formed by the initial oxidation and their distribution, the role played by nitrogen during annealing, nor the consequent changes at the interface are fully understood.

Herein, we exploit the strength of LE μ SR to study the impact of thermal oxidation and postoxidation annealing (POA) in a NO environment on the SiO₂-SiC interface in a depth-resolved manner. A detailed quantification of the carrier concentration near the surface of the NO annealed samples is performed, revealing an unintentional doping during the annealing and the variation of carrier concentration from the interface towards the SiC bulk. Further, a thin layer of metal is deposited on the oxide to fabricate a metal-oxide-semiconductor (*M-O-S*) capacitor, and the resulting changes in carrier concentration due to the potential variation at the surface of the semiconductor are studied using LE μ SR.

II. METHODOLOGY

For the experiments, *n*-type, nitrogen-doped 4H-SiC sample wafers with 30- μ m-thick epitaxial layers are employed. Each sample in the set underwent thermal oxidation, two of the samples are exposed to a POA treatment in NO ambient, and one sample in Ar ambient. The doping density of each sample is approximately $2.6 \times 10^{15} \text{ cm}^{-3}$. A thin layer of SiO₂ is deposited (using PECVD) on top of the thermal oxide to reach a total thickness of 100 nm, such that the SiC-SiO₂ interface lies at the same distance from the surface for each sample. In a second set, a thin layer of aluminum (Al) is deposited on top of the thermal oxide instead of the PECVD oxide to reach a total thickness of 100 nm. An overview of the sample-processing parameters is presented in Table I.

The samples are characterized with low-energy muon-spin-rotation spectroscopy, capacitance-voltage (*C-V*) method and deep-level transient spectroscopy (DLTS). A theoretical study is performed using density-functional-theory (DFT) calculations to investigate the preferred position of nitrogen in the 4H-SiC lattice and its proclivity for motion under the relevant annealing conditions.

A. LE- μ SR

Positively charged muons (μ^+) used in a μ SR experiment are almost 100% spin ($S = 1/2$) polarized. They decay into a positron and two neutrinos with a mean lifetime of 2.2 μ s. The positron is emitted preferentially in the direction of the muon spin at the time of decay and carries the information about the time evolution of the muon spin polarization under the influence of the local and external magnetic fields. The LE μ SR experimental setup is illustrated in Fig. 1(a).

In a conventional μ SR experiment, the μ^+ is implanted at a high energy of around 4 MeV, which leads to a penetration depth of hundreds of μ m to a few mm into the material. In order to study the SiO₂-SiC interface, the μ^+ are slowed down using a moderator [19] and then reaccelerated to energies from 1–28 keV. This energy

TABLE I. Description of sample preparation and processing steps. Deposition is performed using PE-CVD for SiO₂ and PVD for Al.

Sample name	Oxidation parameters	Oxide thickness	POA parameters	Deposition
1300x	32 min at 1300 °C	48 nm	...	SiO ₂ , 52 nm
1300NO1150	30 min at 1300 °C	48 nm	70 min at 1150 °C in NO	SiO ₂ , 52 nm
1300NO1300	28 min at 1300 °C	56 nm	70 min at 1300 °C in NO	SiO ₂ , 44 nm
1300Ar1300	32 min at 1300 °C	48 nm	70 min at 1300 °C in Ar	SiO ₂ , 52 nm
1300x-Al	32 min at 1300 °C	48 nm	...	Al, 52 nm
1300NO1150-Al	30 min at 1300 °C	48 nm	70 min at 1150 °C in NO	Al, 52 nm
1300NO1300-Al	28 min at 1300 °C	56 nm	70 min at 1300 °C in NO	Al, 44 nm
1300Ar1300-Al	32 min at 1300 °C	48 nm	70 min at 1300 °C in Ar	Al, 52 nm

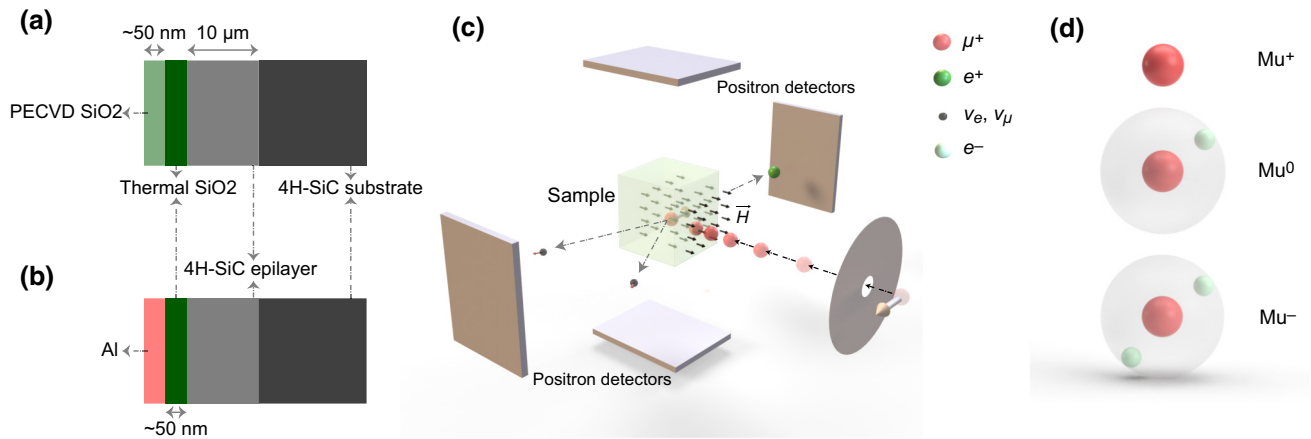


FIG. 1. Schematic diagram of the (a) oxide-semiconductor, (b) metal-oxide-semiconductor samples. (c) Illustration of the μ SR experimental setup. Spin-polarized muons with their spins pointing perpendicular to the direction of motion are implanted in the sample. Under the influence of the local and the applied external magnetic fields, the muon precesses and decays with a mean lifetime of 2.2 μ s into a positron and two neutrinos. The decay positrons are detected using the positron detectors. (d) The three possible states of muonium inside the semiconductor.

range translates to tunable mean implantation depths between 10 and 150 nm in SiC. Using low-energy muons a detailed depth profile can be obtained for the interface and the near interface regions of the oxide-semiconductor structure. Muon implantation profiles in the SiO₂-SiC system are shown in Fig. 2(a). Using one or two Gaussian fits, the mean implantation depth and the FWHM of each implantation profile is extracted and is shown in Fig. 2(b). The implication of the nonzero FWHM is that the μ SR signal measured has contributions from the regions in the vicinity of the mean implantation depth at that energy.

When the μ^+ is implanted in the material, it undergoes inelastic scattering processes where it is decelerated and loses most of its energy within 10 picoseconds and creates a track of ionization electrons. As the energy of the μ^+ is reduced, fewer electrons are ionized and below a

few keV, no further ionization track electrons are generated. The μ^+ then loses its energy by charge-exchange cycles and comes to rest within a picosecond as Mu^+ or Mu^0 . [22] Mu^0 is a hydrogenlike bound state of a μ^+ with an e^- . It behaves like a light isotope of hydrogen inside the semiconductor and can exist in three differently charged configurations: the paramagnetic neutral Mu^0 , and the charged diamagnetic negative (Mu^-), or positive (Mu^+) muonium configurations.

In a hole-rich environment, the Mu^0 can capture a hole to form Mu^+ , whereas in an electron-rich environment, Mu^0 can capture an electron to form Mu^- . The three charge states of the muonium atom are illustrated in Fig. 1(b). The electron-hole capture rate of Mu^0 must be significantly higher than the muon lifetime to be visible in the μ SR spectrum. Slower transitions depolarize quickly and appear as missing diamagnetic fraction.

Due to the hyperfine interaction between the bound e^- and the μ^+ , the precession frequency of the muon spin in the paramagnetic Mu^0 in a transverse magnetic field B is considerably different to the Larmor precession frequency $\omega_D = \gamma_D \times B$ of the muon spin in its diamagnetic states (γ_D is the gyromagnetic ratio of the muon). In low transverse magnetic fields ($B \leq 1$ mT) the transition frequencies between the triplet states in Mu^0 with isotropic hyperfine coupling are degenerate. Here, the triplet Mu^0 precession can be observed at a frequency $\omega_{\text{Mu}} = \gamma_{\text{Mu}} \times B$, where the gyromagnetic ratio γ_{Mu} of the triplet state is about 103 times larger than the gyromagnetic ratio γ_D of the muon.

At higher fields, the transition frequencies between the triplet states split [1]. The precession frequencies of Mu^0 at $B > 4$ mT cannot be resolved by the spectrometer at the LE μ SR setup and appear as a loss of signal. Therefore, all

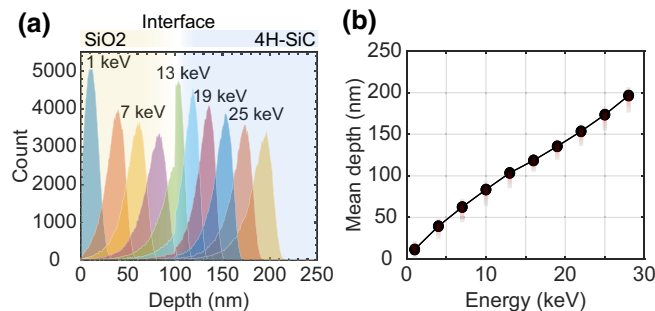


FIG. 2. (a) Muon implantation profile for energies between 1 and 28 keV, simulated with TRIM.SP [20,21]. (b) The calculated mean depth for each implantation energy is indicated with circles and the associated spread of the muon-implantation profile is indicated by the shaded gray bars.

measurements in this work are performed at a low field of 0.5 mT.

The large difference between the precession frequencies of Mu^0 and Mu^+/Mu^- allows us to readily resolve the paramagnetic and the diamagnetic components. In low transverse magnetic fields with degenerate triplet Mu^0 precession frequencies, the muon decay asymmetry $A(t)$ is given by

$$A(t) = A_D \exp(-\lambda_D t) \cos(\omega_D t + \phi_D) + A_{\text{Mu}} \exp(-\lambda_{\text{Mu}} t) \cos(\omega_{\text{Mu}} t + \phi_{\text{Mu}}), \quad (1)$$

where A_D and A_{Mu} are the decay asymmetries of the diamagnetic and the paramagnetic states with precession frequencies ω_D and ω_{Mu} , respectively, and λ_D and λ_{Mu} are the corresponding depolarization rates. The initial phases ϕ_D and ϕ_{Mu} of the diamagnetic and paramagnetic μSR signals are determined by the position of a specific positron detector with respect to the initial muon spin direction. If the diamagnetic state forms from a neutral precursor state—where the muon spin moves in the opposite direction to the Larmor precession—a negative phase shift of ϕ_D with respect to the muon Larmor precession can be observed for the diamagnetic signal, if the transition rate to the diamagnetic state is on the order of hundreds of MHz [3, 11].

The longer the muon stays in the precursor Mu^0 state, the more negative the phase becomes. Within a semiconductor sample, narrow regions with different carrier concentrations strongly impact the measured asymmetry and phase. In n -type regions of a semiconductor, the Mu^0 state can capture a free electron to form the diamagnetic Mu^- state. The higher the density of free electrons, the faster is the capture process, resulting in an increase of the measured A_D and a corresponding change of the negative phase shift as a function of free carrier density. Therefore, the diamagnetic asymmetry and phase of the μSR signal strongly depend on the carrier concentration. It is worthwhile to note that the muon may change the local electrical environment of the host material, for example, by capturing localized electrons at defects as demonstrated in Ref. [13]. Herein, we are exploiting this tendency of the muon to interact with the material to monitor defect formation after thermal oxidation and quantify the charge-carrier concentration (as it has been demonstrated in Ref. [11]).

B. Electrical characterization

Thermal oxidation of SiC is known to create electrically active defects at and near the interface. These defects are commonly studied with C - V analysis to gauge their concentration and energy levels in the band gap [23]. Circular 200-nm-thick aluminium (Al) contacts of diameter varying between 200 to 600 μm are deposited on top of the thermal oxide using an e -beam evaporator to create a M - O - S

structure. A 100-nm-thick layer of Ni is deposited on the C face to get a good Ohmic contact. Quasistatic and high-frequency (2-MHz) C - V measurements are performed on the M - O - S capacitors and used to calculate the density of interface traps (D_{it}).

The samples are also characterized using DLTS using a reverse bias of 0 V and a pulse voltage of -5 V. A pulse width of 100 ms and period width of 500 ms are used for each measurement. The DLTS signal refers to the coefficient of the sine term (b_1) in the Fourier series of the deep-level transient Fourier spectroscopy (DLTFS) [24].

In the experiment, we focus on the N-related defects in the SiC and have therefore chosen a temperature range from 25 to 60 K.

C. Density-functional-theory calculations

DFT calculations as implemented in the Vienna *ab initio* simulation package or VASP code [25, 26] are performed to investigate defect energetics and kinetics for nitrogen incorporation into the 4H-SiC lattice. The lattice parameters are obtained by relaxing the 4H-SiC unit cell using the hybrid Heyd-Scuseria-Ernzerhof HSE06 functional [27] until the forces are below $0.005 \text{ eV } \text{\AA}^{-1}$, yielding a band gap of 3.17 eV close to the experimental value. 400-atom and 576-atom 4H-SiC supercells are constructed from the relaxed unit cell and defects created by adding and removing atoms. Defect relaxations are performed using 576-atom supercell, the GGA-level Perdew-Burke-Ernzerhof (PBE) functional [28] and a $2 \times 2 \times 2$ \mathbf{k} mesh. The convergence criterion for the electronic self-consistent loop is set to $1 \times 10^{-6} \text{ eV}$ for a geometric relaxation criterion of $0.01 \text{ eV } \text{\AA}^{-1}$ maximum forces and a 450-eV energy cutoff. Defect energetics are obtained self-consistently by single-shot calculations for the same supercell and parameters using the HSE06 functional and Γ -only \mathbf{k} -point sampling.

Formation energy diagrams for point defects are constructed according to Ref. [29]:

$$E^f(q) = E_{\text{defect}}^{\text{total}}(q) - E_{\text{supercell}}^{\text{total}} - \sum_i n_i \mu_i + q(E_V + E_F) + E^{\text{FNV}}, \quad (2)$$

where $E_{\text{defect-supercell}}^{\text{total}}$ refers to the total energy of the defective and pristine supercells, respectively, n_i is the number of atoms added ($n_i > 0$) or removed ($n_i < 0$) from the supercell to create the defect, and μ_i is the chemical potential for each species (Si, C, N). Formation energy diagrams are computed in the Si-poor and C-rich limit. Chemical potentials for Si and C are determined from the total energy per atom of the unit cell of Si and diamond, respectively, while μ_N is obtained from Si_3N_4 . The unit cells to obtain μ_i for Si, C, and N are relaxed using HSE06, 700-eV energy cutoff, a \mathbf{k} -mesh density of 4, and for a geometric relaxation criterion of $0.005 \text{ eV } \text{\AA}^{-1}$ maximum forces.

Furthermore, E_V refers to the valence-band maximum and E_F is the Fermi-level position relative to E_V . The total energies for charged defects are corrected according to the Freysoldt-Neugebauer-van de Walle (FNV) correction scheme [30] where E^{FNV} is a correction term to account for the use of charged and finite-sized supercells.

Defect migration is studied using the nudged elastic band (NEB) method [31]. NEB calculations take as input two fixed structures: the initial and final state of the migration. A chain of intermediate structures, or “images,” is then formed as a first guess along the migration path. The images are connected via spring forces to keep them sufficiently distinct from one another and optimized collectively. The NEB calculations herein are performed for interstitial nitrogen entering the Si vacancy in neutral and negative charge state using 11 intermediate images, a 450-eV energy cutoff, Γ -only \mathbf{k} -point sampling and the PBE functional. The forces are relaxed until the maximum force is below 0.05 eV \AA^{-1} for the migration paths.

Hydrogen is often used in DFT calculations to emulate the behavior of positively charged muons. Previous works [13,32–34] have studied the preferred sites of H (analogous to Mu) in 4H-SiC and found that H^+ prefers a configuration antibonding to C (AB_C), while H^- occupies the tetrahedral T_{Si} site in the lattice. Hence, the calculation for the muon site is not repeated in this work. Instead, we consider the behavior of nitrogen in the 4H-SiC lattice and its interaction with different defect types.

III. RESULTS AND DISCUSSION

The two sets of samples described in Table I are studied with LE μSR . The experiments are performed at a low magnetic field of 0.5 mT and at 10 and 260 K. By combining low- and high-temperature measurements the impact of charge carriers on the μSR signal can be clearly distinguished.

A. LE μSR study of oxide-semiconductor samples

Figure 3 compares the LE μSR data at 10 K for thermally oxidized samples that experienced different POA conditions. The light-yellow region represents the thermally grown SiO₂ whereas the blue region is the 4H-SiC epilayer. The shaded region inbetween represents the oxide-semiconductor interface. The diamagnetic asymmetry (A_D) is plotted against the mean depth extracted from the implantation profiles of the muons. The FWHM associated with the mean depth is shown using the shaded bars.

In thermally grown SiO₂, Mu^0 formation is supported due to high structural order and therefore a typical A_D signal [35] between 0.05 to 0.06 is observed across the samples. In 4H-SiC, at 10 K, a freeze out of carriers is expected. Due to the lack of carriers, the implanted muon has a low probability to form the diamagnetic states Mu^+

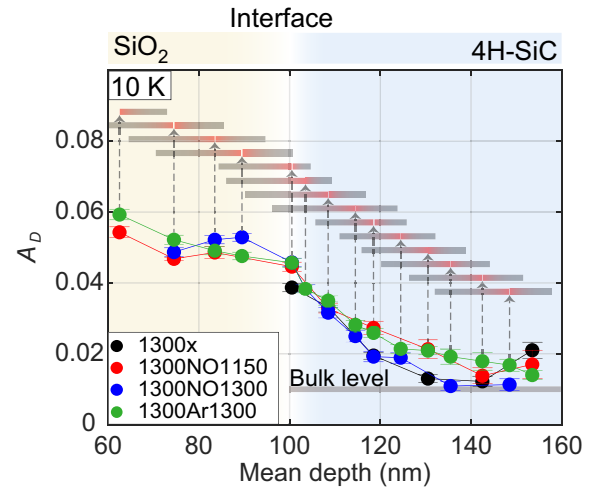


FIG. 3. Diamagnetic asymmetry A_D as a function of mean depth measured at 10 K and 0.5 mT.

or Mu^- . The diamagnetic asymmetry therefore drops to even smaller values after the interface and only slight differences in the muon behavior can be observed across the four samples.

The μSR data recorded at 260 K are shown in Fig. 4. The A_D is no longer similar for the four samples that underwent different POA procedures. Instead, substantial differences across the set are observed, in addition to remarkable changes compared to the 10-K case. The slight increase in diamagnetic asymmetry for the nonannealed sample (1300 \times) compared to the 10-K data can be attributed to the ionization of the nitrogen dopants at 260 K. Moreover, a remarkable increase can be observed for the NO-annealed samples compared to the data recorded at 10 K and at 260 K for the samples that did not receive a POA in NO (1300 \times , 1300Ar1300). Since all the samples have very similar initial doping densities the semiconductor doping itself cannot explain the large difference observed in the diamagnetic signals in Fig. 4(a).

The bulk level shown in Figs. 3 and 4(a) as reference is taken from the μSR data of an unprocessed, low-doped n -type 4H-SiC sample [35]. From the A_D signal in SiO₂, it can be observed that close to the interface the diamagnetic signal for both the NO-annealed samples is slightly higher than the nonannealed and the Ar-annealed samples. Due to the nonzero FWHM of the muon-depth profile [indicated in Fig. 4(d)], the muon response measured close to the interface has contributions from the neighboring layer. In order to minimize the impact of the spread of the muon-depth profile on the muon response near the interface, we perform a deconvolution of the experimental data and the stopping depth profile of the muons using a multilayer fitting approach that was employed for interfaces in Ref. [35]. The diamagnetic signal extracted from this method is written as A_D^* in the rest of the paper to distinguish it from the measured diamagnetic signal, A_D . The

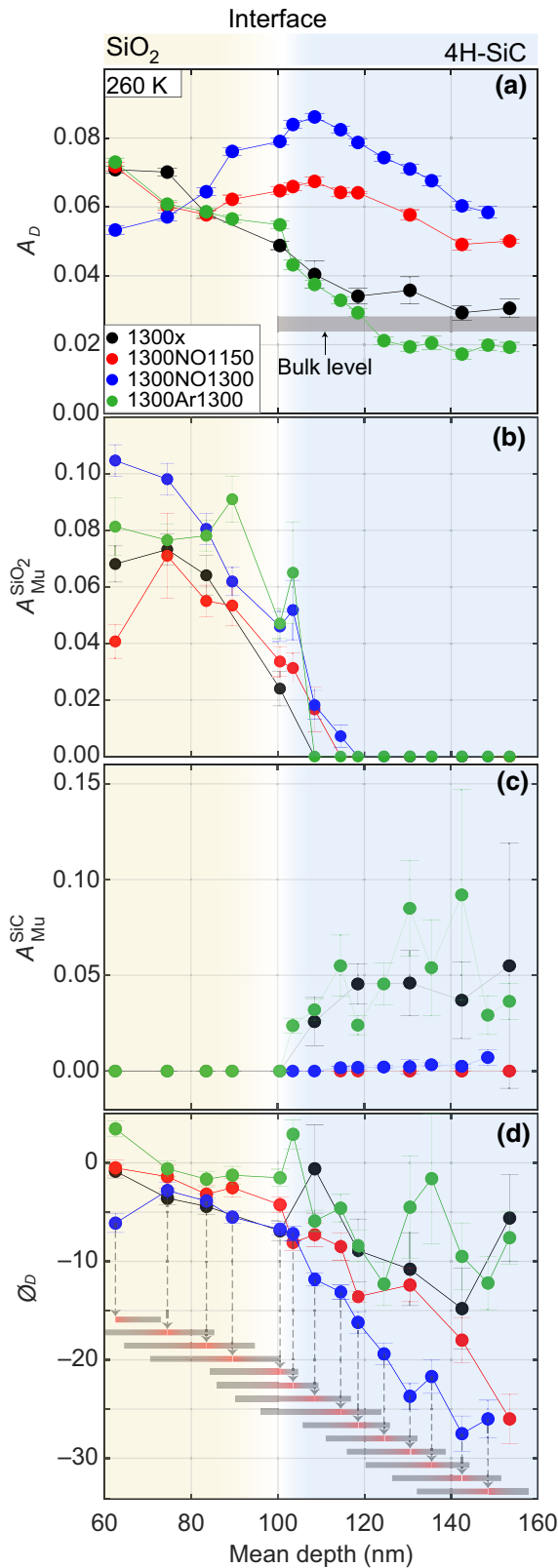


FIG. 4. LE μ SR signals recorded at 260 K and 0.5 mT. (a) Diamagnetic asymmetry (A_D) as a function of mean depth. Paramagnetic asymmetry for the Mu^0 precession at (b) $\omega_{\text{Mu}}^{\text{SiO}_2}$ and (c) $\omega_{\text{Mu}}^{\text{SiC}_a}$, $\omega_{\text{Mu}}^{\text{SiC}_b}$. (d) Phase ϕ_D . The shaded bars at each mean depth shows the FWHM of the muon-implantation profile.

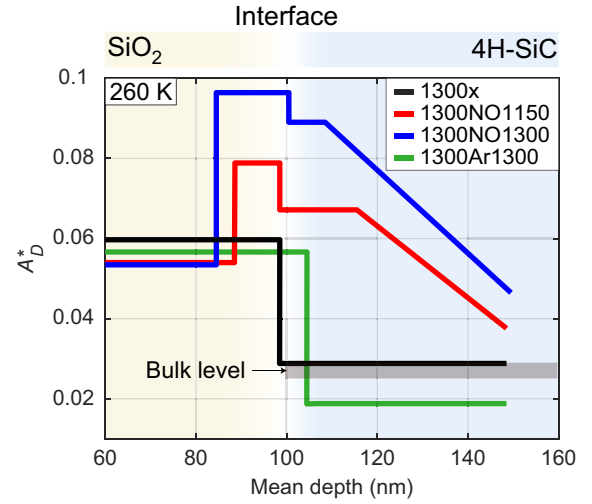


FIG. 5. Diamagnetic asymmetry (A_D^*) extracted by performing the deconvolution of the experimental data and the stopping depth profiles of the muons as described in Appendix A 2.

details of the analysis are shown in Appendix A 2 and the results are shown in Figure 5. It can be seen that in the oxide, far from the interface, the A_D^* signal for the four samples is very similar. For the 1300x and 1300Ar1300 samples, a sharp drop in the A_D^* signal is observed near the interface indicating the transition from SiO₂ to 4H-SiC. However, for the NO-annealed samples, a narrow region of high A_D^* signal is observed in the SiO₂ as we approach the interface. It was shown in Ref. [35] that a high concentration of defects in SiO₂ could be responsible for the increase in the A_D^* signal. Further, a drop in the A_D^* signal is recorded as we transition from the SiO₂ to 4H-SiC but not to the bulk level as observed for the nonannealed (1300x) sample. In SiC, the A_D^* value is high at and near the interface and then begins to drop, still remaining higher than in the nonannealed sample at the end of the probing range around 50 nm from the interface. In other words, the changes imposed on the SiC matrix by the NO annealing remain prominent far beyond the point where the μ SR signal for the 1300x sample reaches the bulk level. In contrast, annealing in an Ar environment results in a significant drop in the A_D^* signal to below the bulk level. The A_D value for the Ar-annealed sample at 260 K is similar to that at 10 K, indicating similar carrier concentration in the first 60 nm of SiC in both cases.

However, a useful conclusion that can be drawn by comparing the A_D^* value for the NO- and Ar-annealed samples is that the increase in the A_D^* signal for NO-annealed samples cannot be attributed to the temperature alone and that NO has to play a pivotal role at the oxide-semiconductor interface.

The paramagnetic Mu^0 has a single precession frequency in SiO₂ ($\omega_{\text{Mu}}^{\text{SiO}_2}$) while it splits into two lines ($\omega_{\text{Mu}}^{\text{SiC}_a}$, $\omega_{\text{Mu}}^{\text{SiC}_b}$) due to an anisotropic hyperfine coupling

in 4H-SiC [35]. Due to the difference in the precession frequencies, the muonium states in SiO₂ and SiC can be distinguished, enabling identification of the interface location. Figure 4(b) shows the paramagnetic signal recorded in SiO₂ ($A_{\text{Mu}}^{\text{SiO}_2}$) precessing at $\omega_{\text{Mu}}^{\text{SiO}_2}$. For 1300× and 1300Ar1300 the $A_{\text{Mu}}^{\text{SiO}_2}$ signal reduces upon approaching the interface and drops to zero inside the semiconductor. However, a small yet non-negligible $A_{\text{Mu}}^{\text{SiO}_2}$ is observed in 4H-SiC for the NO-annealed samples. Due to the nonzero FWHM of the muon-implantation profile [as indicated by the horizontal bars in Fig. 4(d)], a fraction of implanted muons arrive in the SiO₂ and can be responsible for the observed $A_{\text{Mu}}^{\text{SiO}_2}$ signal in the SiC region.

Figure 4(c) shows the paramagnetic asymmetry ($A_{\text{Mu}}^{\text{SiC}}$) recorded for the Mu⁰ inside the SiC. This signal is absent in the SiO₂ and rises behind the SiO₂-SiC interface. Using the paramagnetic signals $A_{\text{Mu}}^{\text{SiC}}$ and $A_{\text{Mu}}^{\text{SiO}_2}$, the two regions of the oxide-semiconductor sample can be clearly identified, the interface can be located and the thickness of the oxide can be estimated. In the case of the nonannealed and Ar-annealed samples, a sharp rise of the $A_{\text{Mu}}^{\text{SiC}}$ signal [Fig. 4(c)] at a mean depth of 100 nm confirms the position of the interface and consequently the thickness of the oxide.

The dependence of the paramagnetic asymmetry on the annealing conditions follows a different pattern in the SiC region as demonstrated by the $A_{\text{Mu}}^{\text{SiC}}$ signal in Fig. 4(c). The 1300× and 1300Ar1300 samples exhibit similar behavior while the contrast is stark to the case after NO annealing. For the NO-annealed samples almost no Mu⁰ precession is observed, indicating that the fraction of the implanted muons forming Mu⁰ quickly transforms to Mu⁻ or quickly depolarizes due to the interaction with free charge carriers [3,35]. Additionally, for samples annealed in the NO environment we observe that in 4H-SiC, the A_D reduces with depth, whereas the paramagnetic signal is close to zero. Therefore, the total recorded asymmetry along the depth of the sample gradually reduces: in the presence of a high concentration of e^- , the Mu⁰ either forms Mu⁻ or undergoes an electron-spin exchange with the free carriers, resulting in a fast depolarization of the signal. Such a signal cannot be captured by our equipment due to the limited resolution and appears as a missing diamagnetic fraction. A sharp reduction in phase is recorded, see Fig. 4(d), indicating that the muon transformed to the diamagnetic state from a neutral precursor state [11].

The changes in muon response as a function of annealing conditions have two potential causes: (i) differences in defect distribution before and after POA, and (ii) differences in carrier concentration.

In order to access the sensitivity of μSR to the defects in 4H-SiC, Woerle *et al.* [12,13] showed that the presence of carbon vacancies (V_C) in n -type 4H-SiC leads to an observable increase in the diamagnetic signal due to the formation of Mu⁻ by electron capture of a neutral precursor state at a

carbon vacancy, if the V_C concentrations $n_{V_C} > 10^{17} \text{ cm}^{-3}$, while the Mu⁰ precession signal remains observable for $n_{V_C} \sim 10^{18} \text{ cm}^{-3}$.

However, thermal oxidation is known to reduce the V_C concentration in SiC and it was shown that the carbon interstitials generated during thermal oxidation can diffuse into the bulk and passivate this lifetime-limiting defect [36,37]. Therefore, the observed increase in the A_D signal in 4H-SiC after NO annealing cannot be attributed to the presence of V_C .

The presence of silicon vacancies (V_{Si}) in 4H-SiC has the opposite impact on the diamagnetic signal [13]. *Ab initio* calculations revealed that the V_{Si} -Mu⁰ complex is energetically more favorable than isolated V_{Si} and leads to a reduction of A_D . V_{Si} has been theorized to be present at and near the SiC-SiO₂ interface after thermal oxidation. With spin-dependent recombination (SDR) studies, signatures were found suggesting that the V_{Si} is a key contributor to the density of interface traps (D_{it}) [38,39]. During the thermal-oxidation process, Si from the SiC matrix is expected to diffuse outwards and react with the incoming oxygen to form the oxide layer [40,41], pointing towards the presence of V_{Si} near the interface. Considering Fig. 4(a), a drop in the A_D signal to the bulk level for 1300× and below the bulk level for 1300Ar1300 indicate a high concentration of V_{Si} near the interface for the nonannealed and Ar-annealed samples.

POA in NO environment is known to significantly reduce the D_{it} [18] when compared to POA in an Ar environment. The D_{it} measured for the four samples are shown in Fig. 6 and exhibit the expected behavior. Assuming that the V_{Si} created by thermal oxidation do indeed have a significant contribution to the D_{it} , a reduction in the D_{it} after

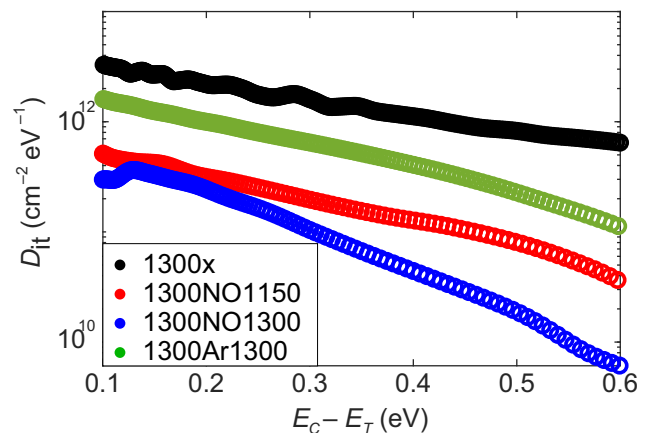


FIG. 6. Density of interface traps D_{it} extracted using the C - V method. E_C is the conduction band edge and E_T is the energetic position of the trap level in the band gap. The non-annealed sample (1300×) has a significantly higher D_{it} when compared to the NO annealed samples (1300NO1150 and 1300NO1300).

POA in the NO environment means that the nitrogen travels through the oxide and passivates the defects at and near the interface. Additionally, nitrogen is likely incorporated into the SiC matrix resulting in a thin region of high carrier concentration [42]. Scanning capacitance microscopy revealed doping levels of around $5 \times 10^{17} \text{ cm}^{-3}$ for samples annealed in N_2O [43] in the region close to the interface. The bulk doping level for the SiC is approximately $5 \times 10^{15} \text{ cm}^{-3}$. Annealing in a NO environment therefore has two implications. Firstly, defect passivation by N leads to a reduction of the interface trap concentration. The reduction of the anticipated Si vacancies near the interface region would result in an enhancement of the diamagnetic asymmetry signal according to the findings of Ref. [13]. Secondly, nitrogen introduced by NO annealing migrating through the oxide layer would create a region of high carrier concentration close to the interface if N occupies a substitutional lattice site in the SiC. The increased A_D signal for the NO-annealed samples [Figs. 4(a) and 5] is therefore likely a result of both of these processes. The presence of residual V_{Si} after NO annealing is still possible but may be overshadowed in the muon data by the large increase in carrier concentration.

The hypothesis that the muon signal in Fig. 4 is responding to an enhanced carrier concentration caused by the NO anneal depends on the nitrogen atoms (i) being able to traverse the SiO_2 layer and migrate up to hundred nanometers into the SiC crystal and (ii) being incorporated on a lattice site, hence, contributing to the charge-carrier density. Figure 7(a) shows the recorded DLTS signal for the four samples 1300 \times , 1300Ar1300, 1300NO1150, and 1300NO1300. The donor level assigned to substitutional N in the pseudocubic configuration, $N_C(k)$ [44–49], is observed for all the samples at around $100 \pm 5 \text{ meV}$ below the conduction-band edge as shown in Fig. 7(b). Electrical parameters of this defect level for the four samples are shown in Table II. The DLTS peak height is directly related

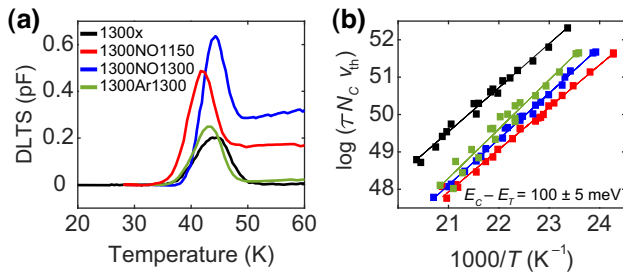


FIG. 7. DLTS spectra for a 0-V reverse bias and a pulse voltage of -5 V . (a) Peaks between 40–45 K are recorded and correspond to an energy level of $100 \pm 5 \text{ meV}$ below the conduction-band edge as shown in (b). This defect is associated with the N donor level at the cubic site. The peak amplitude is higher for the NO-annealed samples indicating the increased N concentration due to the NO annealing.

TABLE II. Electrical parameters of the N-related level measured in DLTS including the energy level below the conduction-band edge, the apparent capture cross section and the ratio of the capacitance transient and the reverse-bias capacitance at the peak in the DLTS signal.

Sample name	$E_C - E_T$ (eV)	Capture cross section (cm^2)	$\Delta C/C_R$
1300 \times	0.098	6.1×10^{-14}	6.7×10^{-2}
1300NO1150	0.098	4.1×10^{-13}	9.6×10^{-2}
1300NO1300	0.104	1.3×10^{-12}	1.4×10^{-1}
1300Ar1300	0.105	7.2×10^{-12}	7.3×10^{-2}

to the defect concentration and it can be seen that for the NO-annealed samples the peak height is substantially higher than for the nonannealed and Ar-annealed samples, evidencing the incorporation of N on lattice sites in the SiC crystal during NO annealing. Furthermore, the fact that the N-peak intensity is higher after annealing in NO at $1300 \text{ }^\circ\text{C}$ as compared to the $1150 \text{ }^\circ\text{C}$ case is an indication that the diffusion of N into the SiC increases with temperature. Hence, the DLTS data demonstrates that nitrogen atoms penetrate the oxide layer for the postoxidation annealing temperatures employed herein.

B. Estimation of carrier concentration using LE μSR

It was shown by Prokscha *et al.* [11,50] that for p -type Ge, the capture of holes by Mu^- depends on the concentration and mobility of the holes, and on the hole-capture cross section of Mu^- . In n -type samples, in an analogous way, it is assumed that due to the presence of majority charge carriers (the excess electrons) in the sample, the diamagnetic signal is dominantly due to Mu^- formation by electron capture of Mu^0 . The transition of Mu^0 to Mu^- is dependent on the electron-capture rate by the Mu^0 and is therefore proportional to the electron concentration, which is equivalent to the concentration of ionized donors (N_D^+). Additionally, the process is also dependent on the electron-capture cross section of the Mu^0 (σ_c^e) and temperature (T). With increasing temperature, the donor atoms are more easily ionized leading to an increase in electron concentration, which supports the formation of Mu^- , however, the mobility of the electrons reduces leading to a reduction in the electron-capture rate. Using these parameters the diamagnetic asymmetry is modeled according to

$$A_D(T) = c_1 N_D^+ \sigma_c \left(\frac{T}{300} \right)^{c_2} + c_3, \quad (3)$$

where c_1 , c_2 , and c_3 are fitting parameters. A calibration is performed using LE μSR measurements on N-implanted 4H-SiC samples with a doping density of $1 \times 10^{17} \text{ cm}^{-3}$. The dopant densities are verified experimentally using secondary ion-mass spectrometry (SIMS). More details are shown in Appendix A 3.

Having established the relation between the A_D and N_D^+ using the reference sample and identified the fitting parameters, Eq. (3) can be used to estimate the N_D^+ (and N_D) in narrow regions of a SiC sample by performing a LE μ SR measurement and extracting the A_D in a depth-resolved manner. This method is employed for the two NO-annealed samples both on the measured A_D signal and on the A_D^* signal extracted after the deconvolution performed using the multilayer approach. The doping concentrations (N_D) and N_D^+ determined from the A_D^* are shown in Fig. 8. The N_D and N_D^+ values extracted from the measured A_D signal (not shown) for the 1300NO1300 sample is slightly lower (approximately $1 \times 10^{17} \text{ cm}^{-3}$) than the results shown in Fig. 8. However, we believe that the deconvolution of the experimental data and the muon stopping profile gives a more accurate value of the diamagnetic signal in the system and therefore is used to extract the nitrogen concentration near the interface for the NO-annealed samples.

The dark red and blue curves represent the carrier concentration at 260 K, while the semitransparent, dotted curves show the dopant concentration (N_D) near the interface. In both the NO-annealed samples, a significant increase in the carrier concentration is observed compared to the background doping concentration of approximately $2.6 \times 10^{15} \text{ cm}^{-3}$. The high carrier concentration shows that N is able to diffuse into the SiC to concentrations as high as $2 \times 10^{17} \text{ cm}^{-3}$ in the topmost tens of nanometer close to the SiO₂-SiC interface. The change in carrier concentration after NO annealing compared to the background

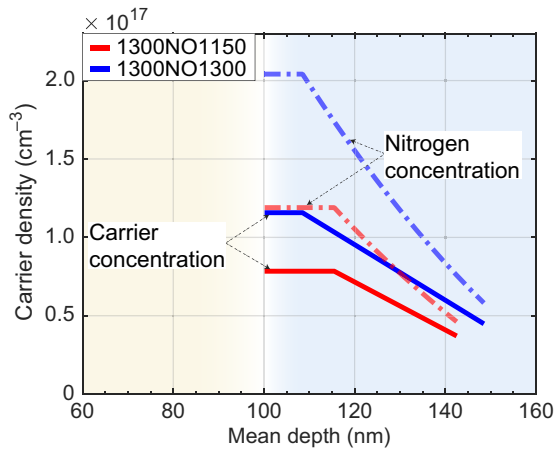


FIG. 8. Extraction of N concentration and the effective carrier concentration near the oxide-semiconductor interface after the POA in NO using the LE μ SR data. The dark (red and blue) curves show the concentration of carriers at 260 K and the semitransparent curves show the concentration of N that must be present to have the calculated free carrier density. The doping concentration is increased by more than an order of magnitude for both the NO-annealed samples compared to the background doping concentration of approximately $2.6 \times 10^{15} \text{ cm}^{-3}$.

doping persists up to at least 50 nm in the SiC. Due to the diffusion of N, the carrier concentration is not uniform and gradually decreases towards the SiC bulk. The impact of this gradual reduction can also be observed in the detector phase recorded for the 1300NO1300 sample in Fig. 4(d). As explained in the previous section, with reducing carrier concentration, the muon stays longer in the Mu^0 precursor state before transforming to Mu^- , leading to a more negative phase.

C. Theoretical defect kinetics

Having established that nitrogen atoms from the NO anneal likely permeate the SiO₂-SiC interface and enter the silicon carbide, two questions remain: (i) where does the nitrogen sit in the 4H-SiC lattice, and (ii) is nitrogen migration in 4H-SiC feasible under the relevant conditions. Formation energy diagrams for various defect species are formed using DFT calculations to address the first question. Figure 9 shows formation energy diagrams for the C and Si vacancies, N on C and Si lattice sites, and the nitrogen split interstitial on a C lattice site. Note that only one lattice-site configuration (hexagonal, h , as opposed to pseudocubic, k), is considered for the nitrogen-related point defects herein. The nitrogen split interstitial is found to inhabit a neutral charge state in n -type and intrinsic 4H-SiC material.

As also found in previous works [51,52], N on the C lattice site (N_C) is more energetically favorable than N on the Si lattice site (N_{Si}) by over 5 eV in n -type 4H-SiC. Moreover, formation of N_C is energetically favorable as compared to V_C , while this is only true for the Si lattice site in p -type material—not in n type. This can be understood in relation to the impact of the nitrogen on the surrounding material. N_C incurs little to no relaxation in the surrounding lattice. Indeed, nitrogen is similar to carbon in the fact

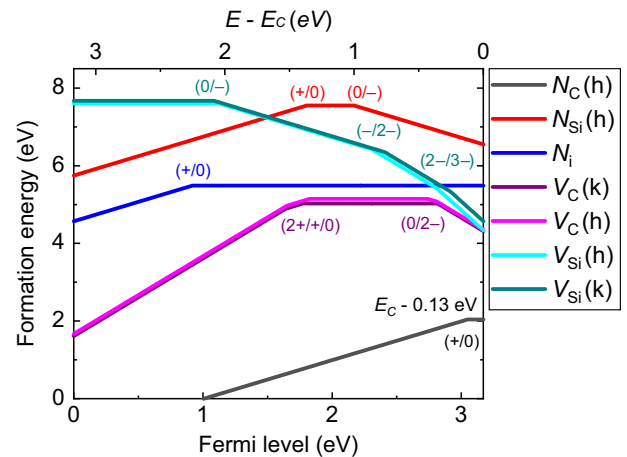


FIG. 9. Formation energy diagrams for nitrogen and Si and C vacancies in 4H-SiC calculated using the HSE06 hybrid functional and 576-atom supercells.

that they have similar atomic radii being nearest neighbors on the periodic table and may exhibit sp^3 -hybrid orbitals. The similarity between the electronic structures of N and C causes little additional energy cost upon replacing one with the other, while nitrogen cannot replace silicon in the Si-C crystal-bonding structure. Hence, N_{Si} causes a displacement of neighboring atoms that comes with an energy cost. In the negative charge state, N_{Si}^- , the nearest-neighbor C atoms to N_{Si} are distorted inwards in the basal plane while the axial C atom experiences an outward relaxation along the c axis. The dopant-site competition for nitrogen in 4H-SiC is therefore expected to result in the vast majority of N atoms residing on the C lattice site [53].

The LE μ SR data clearly demonstrates an increase in carrier concentration near the interface after NO annealing that is attributed to nitrogen-donating electrons to the lattice. Figure 9 confirms that N_C acts as a shallow dopant and contributes electrons to the lattice. N_{Si} , on the other hand, is found to act as a deep-level defect and charge-carrier trap in both p - and n -type material. However, if we assume the presence of Si vacancies after thermal oxidation (as shown in, e.g., Refs. [38,39]), the formation of N_{Si} can, in fact, free electrons to the lattice. The V_{Si} occupies the triply negative charge state in n -type material while N_{Si} is only single negatively charged. Hence, the transformation of V_{Si} into N_{Si} would release charge carriers to the lattice and contribute to an increase in the effective carrier density.

The hypothesis presented in Fig. 8, that nitrogen enters the 4H-SiC lattice to a range of some hundred nanometer, relies on nitrogen being able to migrate in 4H-SiC at 1300 °C during the NO anneal. Previous theoretical studies find activation energy barriers for migration of interstitial nitrogen in the neutral charge state in the 2.6- to 3.0-eV range [54,55]. Figure 10(a) shows an example minimum energy path for neutral interstitial nitrogen, N_i^0 , migrating along the c axis in 4H-SiC calculated herein using the NEB method. The migration barrier is estimated at around 2.2 eV, slightly below previous works, but is likely underestimated due to the use of the PBE functional and Γ -only \mathbf{k} -point sampling [56]. Assuming that the diffusivity of N_i is given by $D = D_0 \exp(-E_A/k_B T)$, the diffusion length is given by $l = \sqrt{D\tau}$, and the prefactor for diffusion is $D_0 \sim 0.001 \text{ cm}^2 \text{ s}^{-1}$ [57], the diffusion length for N_i ranges from around 300 nm to 1.4 μm for activation energies of 3.0 and 2.6 eV, respectively, for a NO anneal at 1300 °C for 70 min (see Table I). Hence, the migration of N within the 4H-SiC is deemed feasible herein during the POA in NO—provided that the N atoms are able to traverse the barrier between the SiO_2 and 4H-SiC, the strength of which is unknown.

The higher-energy cost for N to occupy a Si site as compared to a carbon site leaves the question of whether N_{Si} defect formation is at all feasible. Assuming that a N atom sits in an interstitial site close to the V_{Si} , we find that the

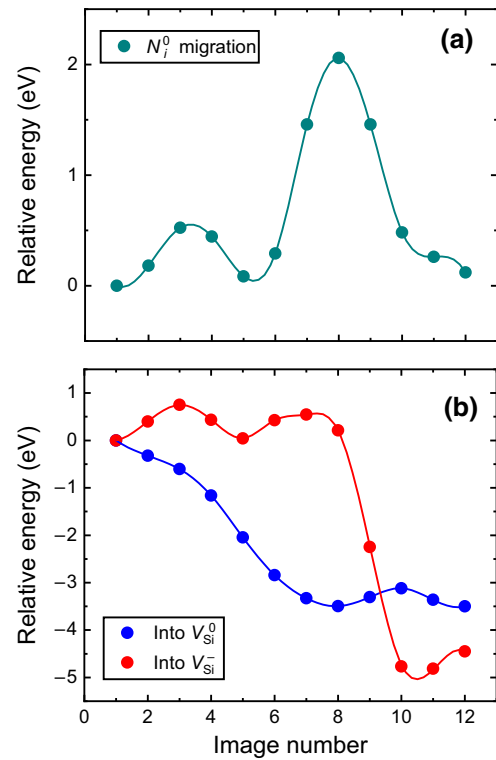


FIG. 10. Minimum energy paths calculated using the NEB method and PBE functional for the (a) neutral N_i migrating along the c axis of 4H-SiC (576-atom supercell) and (b) N_i entering the V_{Si} in the neutral (576-atom supercell, blue circles) and negative (400-atom supercell, red triangles) charge states.

defect complex N_{Si} is lower in energy by as much as 3.7 to 4.2 eV depending on the charge state, see Fig. 9). In this case, where the V_{Si} and the N_i are both already present and in close proximity, the formation of N_{Si} is clearly energetically favorable.

Figure 10(b) shows the migration energy paths of N_i entering the neutral $V_{Si}(h)$ within the basal plane (blue circles) and the negative $V_{Si}(h)$ along the axial direction (red triangles). For both cases there is a substantial energy gain for the transformation to occur, and there is only a small energy barrier of approximately 1.0 eV for the transformation $N_i + V_{Si} \rightarrow N_{Si}$ for the negative charge state, and none at all for the neutral charge state. Note that the defect geometries along the pathways with energies lower than the final structure are an artificial result of the use of the Γ -point only for \mathbf{k} -point sampling for the NEB calculations, while a $2 \times 2 \times 2$ \mathbf{k} mesh is employed for the original structural relaxation.

The results discussed so far demonstrate that (i) N on both the C and Si lattice sites can contribute to the increase in carrier density observed after NO annealing, (ii) N migration in 4H-SiC is feasible under the studied POA conditions, and (iii) the formation of N on Si site is possible provided that both N_i and V_{Si} are present and in

close proximity. The other possible mechanism for nitrogen to provide electrons to the lattice is that the migrating N_i spontaneously kicks out a C atom from a lattice site according to the reaction pathway $N_i + C_C \rightarrow N_C + C_i$. This mechanism was not studied herein but presents an alternative pathway to the formation of N_{Si} considering the much larger energy gain for N to sit on a C compared to a Si lattice site (see Fig. 9). Reference [54] considered a related but slightly different reaction, where instead of occupying the V_{Si}, the interstitial N on a split-interstitial C site kicks out a C atom to form the nitrogen-vacancy center and a C split interstitial: $N_i + V_{Si} \rightarrow N_C V_{Si} + C_i$. The corresponding relatively low activation energy of 2.9 eV is comparable to that expected for N_i migration and suggests that the spontaneous formation of N on the C site is a potential candidate for the observed high carrier densities near the SiC-SiO₂ interface (see Fig. 8).

D. LE μ SR study of metal-oxide-semiconductor samples

In a next step, we investigate the impact of adding a thin layer of metal (Al) on top of the thermal oxide in our samples. The implantation profile of the muons and the LE μ SR data for the *M-O-S* samples at 260 K and 0.5 mT are shown in Fig. 11. In the SiO₂ region, a significant increase in the A_D signal is observed. This is a result of the fraction of muons stopping in Al for energies where the mean depth is in the oxide. Since, we expect only a diamagnetic signal with a high $A_D \sim 0.2$ in Al, even a small fraction of muons stopping in the metal could result in a significant rise in the measured signal. However, with increasing implantation energy of the muons, the fraction of muons stopping in the Al layer reduces and beyond the SiO₂-SiC

interface, the fraction of muons stopping in Al is negligible and therefore has no significant impact. The A_D signal for all samples except for the sample annealed in NO at 1300 °C falls below the bulk level for the *M-O-S* capacitor case at mean depths >120 nm, i.e., about approximately 20 nm away from the interface. Interestingly, the A_D values for the 1300x-Al, 1300NO1150-Al, and 1300Ar1300-Al samples at 260 K are very similar to those recorded for the SiO₂-SiC samples at 10 K (see Fig. 3). While for the oxide-semiconductor samples, a low A_D at 10 K is attributed to the lack of charge carriers due to low temperature, a drop in A_D for the *M-O-S* samples at 260 K could be due to the creation of a depletion region near the interface.

Capacitance-voltage (*C-V*) measurements are performed in quasistatic mode and at high frequency to understand the origin of this alleged depletion region and to extract the density of interface traps. Figure 12 shows the normalized high-frequency capacitance data for the samples. The *C-V* data for 1300NO1150 is laterally shifted when compared to the 1300NO1300 data but not stretched, indicating the presence of a higher density of fixed oxide charges but a similar level of D_{it} . This is also seen in the extracted D_{it} shown in Fig. 6, where the defect densities are very similar for the two NO-annealed samples near the conduction-band edge, and differ only beyond $E_C - 0.3$ eV. The absence of a lateral shift for the 1300NO1300 sample in comparison to the ideal CV curve also indicates that the NO annealing at 1300 °C passivates the fixed oxide charges. The *C-V* data for the 1300x sample is further shifted to the right in comparison to the 1300NO1150 sample and is also stretched out indicating a higher density of fixed oxide charges and interface traps when compared to the NO annealed samples. In comparison, the Ar annealed sample has a steeper *C-V* curve but a similar lateral shift.

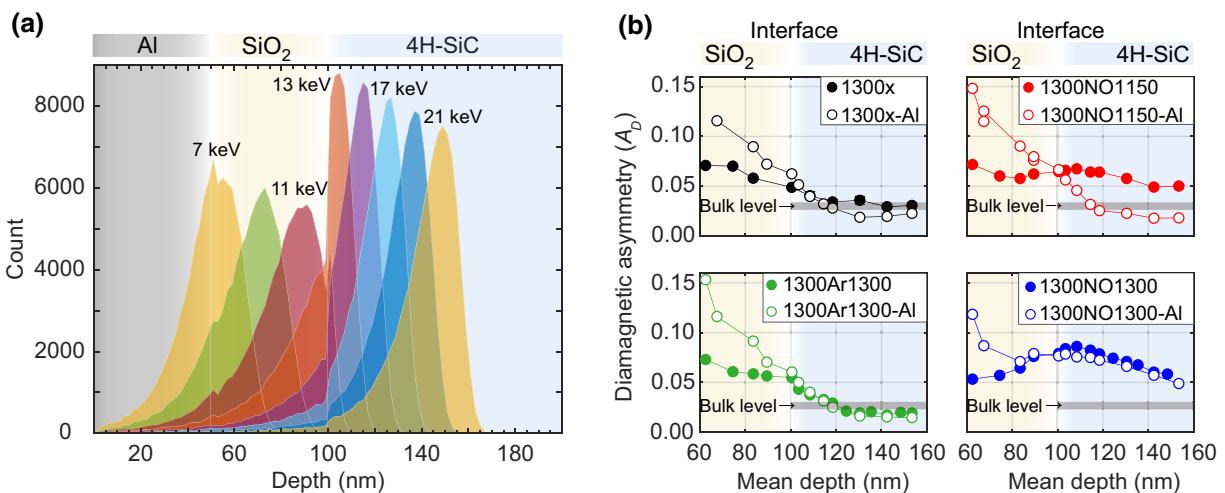


FIG. 11. (a) Implantation profile of muons in the metal-oxide-semiconductor system. (b) A comparison of the A_D signal between the *M-O-S* and the oxide-semiconductor samples at 260 K and 0.5 mT as a function of mean depth. A depletion region is created for the nonannealed, Ar-annealed, and the NO-annealed sample at 1150 °C resulting in a reduced A_D signal in the first 60 nm of SiC. 1300NO1300-Al has a near flat-band condition and shows only a slight reduction in the A_D signal.

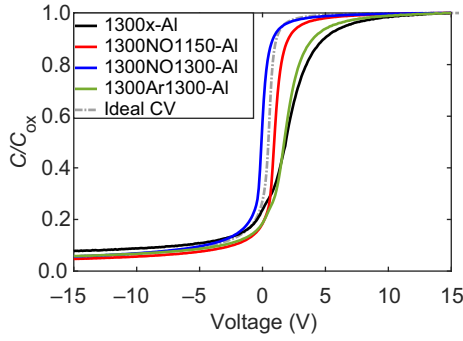


FIG. 12. Normalized high-frequency C - V curves for the M - O - S samples in comparison to the ideal C - V curve. The normalization is performed by using the oxide capacitance (C_{OX}) of the M - O - S capacitor.

This indicates that annealing in an Ar environment helps reduce the D_{it} (see Fig. 6) but the nonannealed and the Ar-annealed samples have similar concentration of oxide charges.

The fixed oxide charges have an impact on the flat-band voltage and consequently on the surface potential at zero bias for the M - O - S capacitors [58]. The flat-band capacitance of the semiconductor is calculated using the Debye length and is then used to extract the flat-band voltage (V_{FB}) of the M - O - S structures. The depletion region width at zero bias (Ψ_{s0} , W_D) and the fixed oxide charges (Q_f) are extracted using the V_{FB} and are shown in Table III. The Ψ_{s0} values for the 1300 \times -Al, 1300NO1150-Al, and 1300Ar1300-Al samples are significantly higher than for the 1300NO1300-Al sample. This translates directly to a large depletion region width near the interface, which would explain the drop in the A_D signal for these samples. For the 1300NO1300-Al sample, a very small Ψ_{s0} implies a near flat-band condition. A depletion region width of 118 nm is calculated for the 1300NO1300-Al sample considering a background doping concentration of $2.6 \times 10^{15} \text{ cm}^{-3}$. However, when we include the increased carrier concentration by more than one order of magnitude to $1.1 \times 10^{17} \text{ cm}^{-3}$ in the topmost 60 nm beneath the SiO_2 -SiC interface, the depletion region width is expected to drop to approximately 20 nm. A small drop in A_D in the first 20 nm recorded for the 1300NO1300-Al sample (see Fig. 11) aligns very well with the C - V measurement and the predicted depletion region width.

A comparison of the LE μ SR results for the sample with and without the metal very clearly demonstrates the correlation between the carrier concentration and the A_D signal. Additionally, the measurement on the 1300NO1300-Al sample helps strengthen the argument that the NO annealing creates a region of high carrier concentration, without which the depletion region would be large enough to strongly impact the A_D signal in the measured approximately 60 nm of SiC. Additionally, the measurements on the M - O - S capacitors show that the variation in charge-carrier concentration due to an external electric field can be studied with LE μ SR, opening doors for a detailed and unprecedented study of accumulation, depletion and inversion in the near interface region of a metal-oxide-semiconductor field-effect transistor (MOSFET) with nanometer depth resolution.

IV. CONCLUDING REMARKS

In this work, we explore the use of LE μ SR to understand the impact of thermal oxidation of SiC and postoxidation annealing in an Ar and NO environment in a depth-resolved manner. With excellent control over the implantation depth of muons, a study of the SiO_2 -SiC interface and near-interface region is performed with nanometer-depth resolution. A comparison of low- and high-temperature measurements reveal that a carrier-rich region is formed near the interface after NO annealing extending up to at least 50 nm into the SiC. Building upon our previous experiments with μ SR and the known affinity of μ^+ to form the $V_{\text{Si}}\text{-Mu}^0$ complex, the increase in A_D for the NO-annealed samples points toward a reduction in the concentration of V_{Si} due to passivation by N and a resulting increased electron concentration. Since a significant drop in the D_{it} is also observed for the NO-annealed samples, our results suggest that V_{Si} is a major contributor to the defects at the SiO_2 -SiC interface.

A quantitative analysis of the carrier concentration near the interface is demonstrated using the diamagnetic signal extracted from the LE μ SR measurements. By controlling the probing depth of the muons, small variations in the carrier concentration due to accumulation or depletion in the material can be studied. A doping concentration of $1 \times 10^{17} \text{ cm}^{-3}$ is estimated close to the interface for the sample annealed at 1300 $^\circ\text{C}$ in NO environment, which drops quickly upon moving into the bulk of SiC. An increase in

TABLE III. Electrical parameters of the M - O - S capacitors.

Sample name	Flat-band voltage (V_{FB})	Surface potential at zero bias (Ψ_{s0})	Depletion width (W_D)	Fixed oxide charges (Q_f)
1300 \times -Al	2.3 V	-0.896 V	608 nm	$-7.46 \times 10^{11} \text{ cm}^{-2}$
1300NO1150-Al	1.1 V	-0.420 V	416 nm	$-2.07 \times 10^{11} \text{ cm}^{-2}$
1300NO1300-Al	0.1 V	-0.034 V	118 nm	$2.08 \times 10^{11} \text{ cm}^{-2}$
1300Ar1300-Al	2.0 V	-0.781 V	360 nm	$-6.11 \times 10^{11} \text{ cm}^{-2}$

the N concentration is also observed in the DLTS measurements. Variations in the shallow N level across the sample set indicate that the N concentration is substantially higher (by a factor of 2–3) for the NO-annealed samples when compared to the nonannealed sample.

Density-functional-theory calculations performed in this work and the literature corroborate the possibility for nitrogen migration some 100 nm in 4H-SiC during the POA in NO. Both N on C and Si sites are found to contribute electrons to the lattice upon defect formation. Hence, two possible pathways are found: interstitial N encounters a Si vacancy and forms the N_{Si} deep-level defect, or migrating N_i spontaneously kicks out a C atom from the lattice to form the N_C shallow dopant and a C split interstitial.

Furthermore, the impact of depositing a metal on the oxide-semiconductor structure to form a *M-O-S* capacitor is investigated using LE μ SR and *C-V* measurements. We observe that a depletion region is created near the interface, which results in a drop of A_D for all the samples. While only a slight reduction is observed for the 1300NO1300 sample due to a narrow depletion region, the A_D for the other samples is reduced below the bulk value indicating a much broader space-charge region.

Of note, with the proper calibration available, LE μ SR proves to be a powerful tool for understanding device interfaces, which are known to impact device operation. Despite the limitations and time constraints for employing the technique, we expect muon spin rotation to provide useful insights into the carrier, dopant, and defect concentrations and distributions in the near-interface region and hence to provide valuable information for the further development of SiC-based devices.

ACKNOWLEDGMENTS

The muon experiments are performed at the μ E4/LEM beamline [59] of the Swiss Muon Source S μ S, Paul Scherrer Institute, Villigen, Switzerland. This work is supported by the Swiss National Science Foundation under Grant No. 192218. The work of M.E.B. is supported by an ETH Zurich Postdoctoral Fellowship. The computations are performed on resources provided by UNINETT Sigma2—the National Infrastructure for High Performance Computing and Data Storage in Norway.

APPENDIX

1. Analysis of the μ SR spectrum

The μ SR spectrum is analyzed using the software MUSRFIT [60]. In the diamagnetic state, where the muon precesses at the Larmor frequency (ω_D), an exponentially damped cosine function is used to fit the data.

$$A(t) = A_D \exp\left[-\frac{1}{2}(\sigma_D t)\right]^2 \times \cos(\omega_D t + \phi_D), \quad (\text{A1})$$

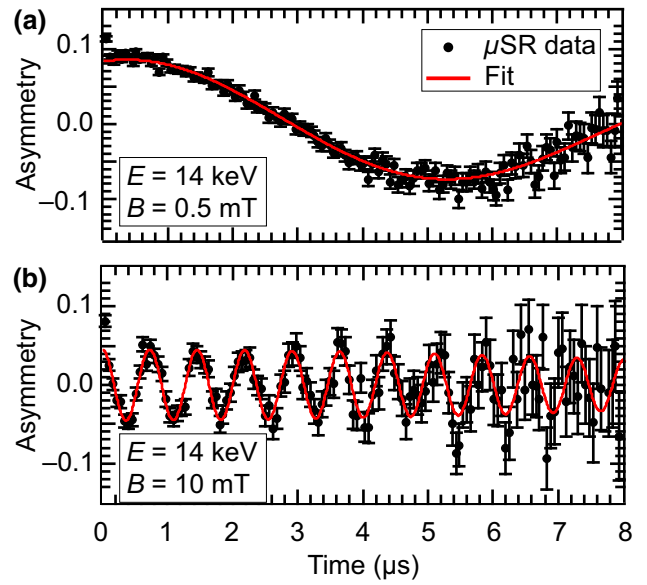


FIG. 13. Diamagnetic asymmetry spectrum in 4H-SiC sample at an implantation energy of 14 keV (a) 0.5 mT and (b) 10 mT.

where A_D is the diamagnetic asymmetry, σ_D is the depolarization rate and ϕ_D is the initial phase of the signal determined by the position of a specific positron detector with respect to the initial muon spin direction. Figure 13 shows a typical μ SR spectrum in the diamagnetic state at 0.5 and 10 mT and the fit created using the Eq. (A1). In the case where both paramagnetic and diamagnetic signals are present in the spectrum (shown in Ref. [35]), a paramagnetic component is added to get the total asymmetry [Eq. (1)]. The fit is then used to extract the paramagnetic and the diamagnetic asymmetries and the corresponding depolarization rates. All the μ SR data presented in this work is analyzed using the MUSRFIT software and the method mentioned above.

2. Depth-dependence modeling

The depth-dependence of the LE μ SR parameters measured as a function of muon-implantation energy E can be obtained by performing deconvolution of the experimental data and the stopping depth profiles of the muons. The fitting method enables the extraction of a depth-dependent model, which is especially useful for the description of systems where the muon-stopping contribution is distributed between layers with distinct muon interaction. To describe the multilayer system, it is assumed in the method developed in Refs. [61,62] that the μ SR parameter, for example A_D , has a characteristic value for each material. Thus, a steplike function is a suitable approximation for the A_D variation as a function of probing depth in the sample. This approach results in a good fit for the data recorded for the 1300 \times and 1300Ar1300 samples, but the changes in SiC due to NO annealing required a more complicated analysis

TABLE IV. Diamagnetic asymmetry A_D for each layer used in the fitting model, and obtained interface position x_{inter} .

Sample Name	A_{SiO_2}	$A_{\text{SiO}_2}^{\text{inter}}$	$A_{\text{SiC}}^{\text{inter}}$	A_{SiC}	x_{inter} (nm)
1300×	0.059(1)	0.028(2)	98(4)
1300NO1150	054(2)	0.078(15)	0.067(1)	0.034(0)	98(2)
1300NO1300	053(1)	0.096(2)	0.089(6)	0.034(0)	100(1)
1300Ar1300	0.056(1)	0.018(1)	105(1)

(see Table IV). The changes of the muon signal in SiC for the 1300NO1300 and 1300NO1150 samples are associated with the presence of free electrons. The effect of the free electron concentration in SiC can be well fitted by adding a region where A_D is described by a linear function of depth x with negative slope:

$$A_D(x) = \begin{cases} A_{\text{SiO}_2} & \text{for } x < a, \\ A_{\text{SiO}_2}^{\text{inter}} & \text{for } a \leq x < b, \\ A_{\text{SiC}}^{\text{inter}} & \text{for } b \leq x < c, \\ A_{\text{SiC}}^{\text{inter}} + \frac{A_{\text{SiC}} - A_{\text{SiC}}^{\text{inter}}}{d-c} \cdot x & \text{for } c \leq x < d, \\ A_{\text{SiC}} & \text{for } x \geq d, \end{cases} \quad (\text{A2})$$

where a , b , c , and d are the depth values used to define the range of each different layer, and A_{SiO_2} , $A_{\text{SiO}_2}^{\text{inter}}$, $A_{\text{SiC}}^{\text{inter}}$, A_{SiC} are the diamagnetic asymmetries in SiO₂, in the near-interface region of SiO₂, in the near-interface region of SiC, and in the low-doped region of SiC, respectively.

The energy-dependent experimental data is fitted with Eq. (A3):

$$A_D(E) = A_{\text{SiO}_2} \times p_{0a}(E) + A_{\text{SiO}_2}^{\text{inter}} \times p_{ab}(E) + A_{\text{SiC}}^{\text{inter}} \times p_{bc}(E) + \int_c^d A(x) \times P(x, E) dx + A_{\text{SiC}} \times p_{d\infty}(E), \quad (\text{A3})$$

where $P(x, E)$ is the muon-stopping probability per unit length, obtained with the TRIM.SP [20,21] simulation, and $p_{ab}(E)$ is the probability that the muon implanted with energy E stops in the range $a < x < b$, calculated by numerical integration:

$$\int_a^b P(x, E) dx. \quad (\text{A4})$$

3. Electron-capture process for the formation of the diamagnetic signal in a N-implanted sample

In a moderately to highly doped n -type 4H-SiC sample, the Mu^0 formed at the end of the ionization track can capture an electron from the semiconductor to form the diamagnetic state Mu^- . Prokscha *et al.* [11,50] showed

that for Ge, the capture of holes by the muonium depends on the concentration of holes, the capture cross section (σ_c^h), and the thermal velocity (v_h) of the carriers. It is further found that the product of v_h and σ_c is proportional to $T^{-2.4}$, indicating that the hole-capture rate by muonium is governed by the mobility of the holes. Using a similar approach for n -type samples, the transition of Mu^0 to Mu^- would also be directly proportional to the density of free electrons (approximately N_D^+), the electron-capture cross section of the Mu^0 (σ_c^e) and the temperature. With increasing temperature, more donor atoms are ionized supporting the transition to the diamagnetic state, but at the same time, the mobility of carriers is reduced, counteracting the electron-capture rate increase due to the increasing electron concentration. In the low-temperature range (<60 K), the electron density is very low and the ionization is smaller than 1% of the doping density. Consequently, A_D is very small and a large fraction of the implanted muons exist in the paramagnetic state as shown in Figs. 14(a) and 14(b). As the temperature is increased, the electron density increases and the transition of Mu^0 to Mu^- is supported. This is evident from the blue region in Fig. 14 where a rapid rise in A_D at the cost of A_{Mu} is observed. Beyond 180 K, more than 50% of the donors are ionized and the sample has a high electron density. However, the increasing temperature also adversely affects the electron-capture rate of Mu^0 , reducing the rate of increase of diamagnetic asymmetry with temperature.

Further, to calculate the N_D^+ in our reference sample, the information of the donor levels is crucial. N-related donor levels in 4H-SiC have been reported in the literature and range from 40–65 meV for the hexagonal site and 85–125 meV for the cubic site [44–47]. In our analysis we choose two donor levels within this range: 50 meV (hexagonal site) and 100 meV (cubic site), with each level occupying half of the dopants. This assumption has a certain error margin due to the spread in the reported values, and a variation in the ratio of $N_C(h)$ to $N_C(k)$ may lead to discrepancies in the calculated carrier concentration. Accounting for the spread of the energy levels from various sources in the literature, a variation of up to 25% can occur in the calculated carrier concentration when comparing the lower and upper bounds for the N-related donor levels: N_{lower} (40 meV, 85 meV) and N_{upper} (65 meV, 125 meV).

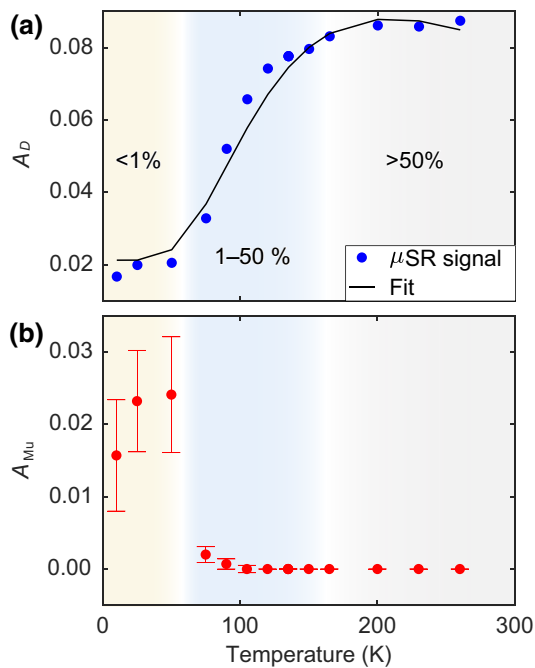


FIG. 14. (a) Diamagnetic asymmetry A_D as a function of temperature T of a 10^{17} cm^{-3} N-implanted sample. The solid line is a fit of Eq. (3) to the data. Three zones of temperature are shown in the figure with low (<1%), medium (1–50%) and high (>50%) degree of donor ionization (b) Paramagnetic asymmetry A_{Mu} is high in the low temperature range but drops quickly to almost zero as the temperature rises beyond 100 K.

Taking into account the impact of the ionization of dopants (N_D^+) and the temperature, A_D can be modeled for the entire temperature range according to Eq. (3) with calibration coefficients c_1 , c_2 , and c_3 . The A_D signal for the 10^{17} cm^{-3} N-implanted sample is used for calibration. The muon implantation energy is kept at 18 keV, which would correspond to a mean depth of approximately 100 nm in the SiC. The sample underwent a postimplantation annealing at 1700 °C for 30 min and is then thoroughly cleaned in 2% HF solution to remove any native oxide before the measurement.

Assuming a constant capture cross section (σ_c^e) of $1 \times 10^{-15} \text{ cm}^2$, and calculating the N_D^+ at each temperature (100% donor activation is assumed), Eq. (3) is solved to get the best fit of the acquired data. The extracted calibration coefficients are $c_1 = 7.08 \times 10^{-4}$, $c_2 = -1.33$, $c_3 = 0.021$.

The recorded A_D and the fit is shown in the Fig. 14(a). Using these coefficients, a very good agreement between the experimental data and the model [Eq. (3)] is observed.

[1] Stephen J. Blundell, Roberto De Renzi, Tom Lancaster, and Francis L. Pratt *Muon Spectroscopy—An Introduction* (Oxford University Press, Oxford, 2021).

- [2] A. D. Hillier, S. J. Blundell, I. McKenzie, I. Umegaki, L. Shu, J. A. Wright, T. Prokscha, F. Bert, K. Shimomura, A. Berlie, H. Alberto, and I. Watanabe, Muon spin spectroscopy, *Nat. Rev. Dis. Primers* **2**, 4 (2022).
- [3] B. D. Patterson, Muonium states in semiconductors, *Rev. Mod. Phys.* **60**, 69 (1988).
- [4] S. F. J. Cox, Muonium as a model for interstitial hydrogen in the semiconducting and semimetallic elements, *Rep. Prog. Phys.* **72**, 116501 (2009).
- [5] I. McKenzie, The positive muon and μSR spectroscopy: Powerful tools for investigating the structure and dynamics of free radicals and spin probes in complex systems, *Annu. Rep. Section C (Phys. Chem.)* **109**, 65 (2013).
- [6] M. Hiraishi, *et al.*, Bipartite magnetic parent phases in the iron oxypnictide superconductor, *Nat. Phys.* **10**, 300 (2014).
- [7] B. A. Frandsen, *et al.*, Volume-wise destruction of the antiferromagnetic Mott insulating state through quantum tuning, *Nat. Commun.* **7**, 12519 (2016).
- [8] F. Pratt, T. Lancaster, P. Baker, S. Blundell, W. Kaneko, M. Ohba, S. Kitagawa, S. Ohira-Kawamura, and S. Takagi, Muon spin relaxation studies of critical fluctuations and diffusive spin dynamics in molecular magnets, *Phys. B: Condens. Matter* **404**, 585 (2009).
- [9] A. J. Drew, C. Niedermayer, P. J. Baker, F. L. Pratt, S. J. Blundell, T. Lancaster, R. H. Liu, G. Wu, X. H. Chen, I. Watanabe, V. K. Malik, A. Dubroka, M. Rössle, K. W. Kim, C. Baines, and C. Bernhard, Coexistence of static magnetism and superconductivity in $\text{SmFeAsO}_{1-x}\text{F}_x$ as revealed by muon spin rotation, *Nat. Mater.* **8**, 310 (2009).
- [10] H. Luetkens, H.-H. Klauss, M. Kraken, F. J. Litterst, T. Dellmann, R. Klingeler, C. Hess, R. Khasanov, A. Amato, C. Baines, M. Kosmala, O. J. Schumann, M. Braden, J. Hamann-Borrero, N. Leps, A. Kondrat, G. Behr, J. Werner, and B. Büchner, The electronic phase diagram of the $\text{LaO}_{1-x}\text{F}_x$ FeAs superconductor, *Nat. Mater.* **8**, 305 (2009).
- [11] T. Prokscha, K.-H. Chow, Z. Salman, E. Stilp, and A. Suter, Direct Observation of Hole Carrier-Density Profiles and Their Light-Induced Manipulation at the Surface of Ge, *Phys. Rev. Appl.* **14**, 014098 (2020).
- [12] J. Woerle, T. Prokscha, A. Hallén, and U. Grossner, Interaction of low-energy muons with defect profiles in proton-irradiated Si and 4H-SiC, *Phys. Rev. B* **100**, 115202 (2019).
- [13] J. Woerle, M. E. Bathen, T. Prokscha, A. Galeckas, H. M. Ayyedh, L. Vines, and U. Grossner, Muon Interaction with Negative-U and High-Spin-State Defects: Differentiating Between C and Si Vacancies in 4H-SiC, *Phys. Rev. Appl.* **14**, 054053 (2020).
- [14] W. J. Choyke and G. Pensl, Physical Properties of SiC, *MRS Bull.* **22**, 25 (1997).
- [15] T. Kimoto and J. A. Cooper, *Fundamentals of Silicon Carbide Technology* (John Wiley & Sons Singapore Pte. Ltd, Singapore, 2014).
- [16] V. Veliadis, in *ESSDERC 2022—IEEE 52nd European Solid-State Device Research Conference (ESSDERC)* (Institute of Electrical and Electronics Engineers (IEEE), Milan, Italy, 2022), p. 31.
- [17] J. Mütting and U. Grossner, in *Materials Science Forum*, Vol. 924 (Trans Tech Publ., Switzerland, 2018), p. 693.
- [18] S. Dhar, S. Wang, J. R. Williams, S. T. Pantelides, and L. C. Feldman, Interface passivation for silicon dioxide layers on silicon carbide, *MRS Bull.* **30**, 288 (2005).

- [19] T. Prokscha, E. Morenzoni, C. David, A. Hofer, H. Glückler, and L. Scandella, Moderator gratings for the generation of epithermal positive muons, *Appl. Surf. Sci.* **172**, 235 (2001).
- [20] W. Eckstein, *Computer Simulation of Ion-Solid Interactions*, Springer Series in Materials Science (Springer, Berlin Heidelberg, 1991).
- [21] E. Morenzoni, H. Glückler, T. Prokscha, R. Khasanov, H. Luetkens, M. Birke, E. M. Forgan, C. Niedermayer, and M. Pleines, Implantation studies of keV positive muons in thin metallic layers, *Nucl. Instrum. Methods Phys. Res., Sect. B* **192**, 254 (2002).
- [22] S. J. Blundell, Muon-spin rotation studies of electronic properties of molecular conductors and superconductors, *Chem. Rev.* **104**, 5717 (2004).
- [23] H. Yoshioka, T. Nakamura, and T. Kimoto, Accurate evaluation of interface state density in SiC metal-oxide-semiconductor structures using surface potential based on depletion capacitance, *J. Appl. Phys.* **111**, 014502 (2012).
- [24] S. Weiss and R. Kassing, Deep level transient Fourier spectroscopy (DLTFS)—a technique for the analysis of deep level properties, *Solid. State. Electron.* **31**, 1733 (1988).
- [25] G. Kresse and J. Furthmüller, Efficient iterative schemes for ab initio total-energy calculations using a plane-wave basis set, *Phys. Rev. B* **54**, 11169 (1996).
- [26] G. Kresse and J. Furthmüller, Efficiency of ab-initio total energy calculations for metals and semiconductors using a plane-wave basis set, *Comput. Mater. Sci.* **6**, 15 (1996).
- [27] J. Heyd, G. E. Scuseria, and M. Ernzerhof, Hybrid functionals based on a screened Coulomb potential, *J. Chem. Phys.* **118**, 8207 (2003).
- [28] J. P. Perdew, K. Burke, and M. Ernzerhof, Generalized Gradient Approximation Made Simple, *Phys. Rev. Lett.* **77**, 3865 (1996).
- [29] C. Freysoldt, B. Grabowski, T. Hickel, J. Neugebauer, G. Kresse, A. Janotti, and C. G. Van de Walle, First-principles calculations for point defects in solids, *Rev. Mod. Phys.* **86**, 253 (2014).
- [30] C. Freysoldt, J. Neugebauer, and C. G. Van de Walle, Fully Ab Initio Finite-Size Corrections for Charged-Defect Supercell Calculations, *Phys. Rev. Lett.* **102**, 016402 (2009).
- [31] H. Jónsson, G. Mills, and K. W. Jacobsen, in *Classical and Quantum Dynamics in Condensed Phase Simulations* (World Scientific, 1998).
- [32] M. Kaukonen, C. J. Fall, and J. Lento, Interstitial H and H₂ in SiC, *Appl. Phys. Lett.* **83**, 923 (2003).
- [33] R. L. Lichti, W. A. Nussbaum, and K. H. Chow, Hyperfine spectroscopy of muonium in 4H and 6H silicon carbide, *Phys. Rev. B* **70**, 165204 (2004).
- [34] M. E. Bathen, A. Galeckas, J. Coutinho, and L. Vines, Influence of hydrogen implantation on emission from the silicon vacancy in 4H-SiC, *J. Appl. Phys.* **127**, 085701 (2020).
- [35] M. I. M. Martins, P. Kumar, J. Woerle, X. Ni, U. Grossner, and T. Prokscha, Defect profiling of oxide-semiconductor interfaces using low-energy muons, *ArXiv:2206.00925* (2022).
- [36] T. Hiyoshi and T. Kimoto, Reduction of deep levels and improvement of carrier lifetime in *n*-type 4H-SiC by thermal oxidation, *Appl. Phys. Express* **2**, 041101 (2009).
- [37] K. Kawahara, J. Suda, and T. Kimoto, Analytical model for reduction of deep levels in SiC by thermal oxidation, *J. Appl. Phys.* **111**, 053710 (2012).
- [38] C. J. Cochrane, P. M. Lenahan, and A. J. Lelis, Identification of a silicon vacancy as an important defect in 4H SiC metal oxide semiconducting field effect transistor using spin dependent recombination, *Appl. Phys. Lett.* **100**, 023509 (2012).
- [39] C. Cochrane, P. Lenahan, and A. Lelis, The effect of nitric oxide anneals on silicon vacancies at and very near the interface of 4H SiC metal oxide semiconducting field effect transistors using electrically detected magnetic resonance, *Appl. Phys. Lett.* **102**, 193507 (2013).
- [40] Y. Hijikata, S. Yagi, H. Yaguchi, and S. Yoshi, in *Physics and Technology of Silicon Carbide Devices*, edited by Y. Hijikata (InTech, 2012).
- [41] Y. Hijikata, Macroscopic simulations of the SiC thermal oxidation process based on the Si and C emission model, *Diam. Relat. Mater.* **92**, 253 (2019).
- [42] G. Liu, A. C. Ahyi, Y. Xu, T. Isaacs-Smith, Y. K. Sharma, J. R. Williams, L. C. Feldman, and S. Dhar, Enhanced inversion mobility on 4H-SiC using phosphorus and nitrogen interface passivation, *IEEE Electron Device Lett.* **34**, 181 (2013).
- [43] P. Fiorenza, F. Giannazzo, M. Vivona, A. La Magna, and F. Roccaforte, SiO₂/4H-SiC interface doping during post-deposition-annealing of the oxide in N₂O or POCl₃, *Appl. Phys. Lett.* **103**, 153508 (2013).
- [44] W. Götz, A. Schöner, G. Pensl, W. Suttrop, W. J. Choyke, R. Stein, and S. Leibenzeder, Nitrogen donors in 4H-silicon carbide, *J. Appl. Phys.* **73**, 3332 (1993).
- [45] T. Kimoto, A. Itoh, H. Matsunami, S. Sridhara, L. L. Clemen, R. P. Devaty, W. J. Choyke, T. Dalibor, C. Peppermüller, and G. Pensl, Nitrogen donors and deep levels in high-quality 4H-SiC epilayers grown by chemical vapor deposition, *Appl. Phys. Lett.* **67**, 2833 (1995).
- [46] J. Pernot, W. Zawadzki, S. Contreras, J. L. Robert, E. Neyret, and L. Di Cioccio, Electrical transport in *n*-type 4H silicon carbide, *J. Appl. Phys.* **90**, 1869 (2001).
- [47] S. Kagamihara, H. Matsuura, T. Hatakeyama, T. Watanabe, M. Kushibe, T. Shinohe, and K. Arai, Parameters required to simulate electric characteristics of SiC devices for *n*-type 4H-SiC, *J. Appl. Phys.* **96**, 5601 (2004).
- [48] L. Gelczuk, V. Kolkovsky, M. Sochacki, J. Szmids, and T. Gotszalk, Origin and anomalous behavior of dominant defects in 4H-SiC studied by conventional and Laplace deep level transient spectroscopy, *J. Appl. Phys.* **127**, 064503 (2020).
- [49] N. Assmann, C. Persson, A. Y. Kuznetsov, and E. V. Monakhov, Fine structure in electronic transitions attributed to nitrogen donor in silicon carbide, *Appl. Phys. Lett.* **119**, 262101 (2021).
- [50] T. Prokscha, Simulation of TF- μ SR histograms in germanium in the presence of cyclic charge state transitions of muonium, *J. Phys.: Conf. Ser.* **551**, 012049 (2014).
- [51] P. Deák, A. Gali, J. Miró, R. Gutierrez, A. Sieck, and T. Frauenheim, in *Silicon Carbide, III-Nitrides and Related Materials*, Materials Science Forum, Vol. 258–263 (Trans Tech Publications, Ltd., Singapore, 1997), p. 739.

- [52] R. Rurali, P. Godignon, J. Rebollo, E. Hernández, and P. Ordejón, First-principles study of *n*-type dopants and their clustering in SiC, *Appl. Phys. Lett.* **82**, 4298 (2003).
- [53] D. J. Larkin, P. G. Neudeck, J. A. Powell, and L. G. Matus, Site-competition epitaxy for superior silicon carbide electronics, *Appl. Phys. Lett.* **65**, 1659 (1994).
- [54] U. Gerstmann, E. Rauls, T. Frauenheim, and H. Overhof, Formation and annealing of nitrogen-related complexes in SiC, *Phys. Rev. B* **67**, 205202 (2003).
- [55] E. Rauls, U. Gerstmann, T. Frauenheim, and H. Overhof, The different behavior of nitrogen and phosphorus as *n*-type dopants in SiC, *Phys. B: Condens. Matter* **340–342**, 184 (2003).
- [56] M. E. Bathen, J. Coutinho, H. M. Ayedh, J. Ul Hassan, I. Farkas, S. Öberg, Y. K. Frodason, B. G. Svensson, and L. Vines, Anisotropic and plane-selective migration of the carbon vacancy in SiC: Theory and experiment, *Phys. Rev. B* **100**, 014103 (2019).
- [57] J. Philibert, *Atom Movements: Diffusion and Mass Transport in Solids*, Monographies de Physique (Editions de Physique, 1991).
- [58] D. K. Schroder, in *Semiconductor Material and Device Characterization* (John Wiley & Sons, Inc., Hoboken, NJ, USA, 2005), p. 319.
- [59] T. Prokscha, E. Morenzoni, K. Deiters, F. Foroughi, D. George, R. Kobler, A. Suter, and V. Vrankovic, The new muE4 beam at PSI: A hybrid-type large acceptance channel for the generation of a high intensity surface-muon beam, *Nucl. Instrum. Methods Phys. Res. Section A* **595**, 317 (2008).
- [60] A. Suter and B. Wojek, Musrfit: A free platform-independent framework for μ sr data analysis, *Phys. Proc.* **30**, 69 (2012).
- [61] H. V. Alberto, R. C. Vilão, R. B. L. Vieira, J. M. Gil, A. Weidinger, M. G. Sousa, J. P. Teixeira, A. F. da Cunha, J. P. Leitão, P. M. P. Salomé, P. A. Fernandes, T. Törndahl, T. Prokscha, A. Suter, and Z. Salman, Slow-muon study of quaternary solar-cell materials: Single layers and *p* – *n* junctions, *Phys. Rev. Mater.* **2**, 025402 (2018).
- [62] A. F. A. Simões, H. V. Alberto, R. C. Vilão, J. M. Gil, J. M. V. Cunha, M. A. Curado, P. M. P. Salomé, T. Prokscha, A. Suter, and Z. Salman, Muon implantation experiments in films: Obtaining depth-resolved information, *Rev. Sci. Instrum.* **91**, 023906 (2020).